



Towards a webcam-based snow cover monitoring network: methodology and evaluation

Céline Portenier¹, Fabia Hüsler², Stefan Härer³, and Stefan Wunderle¹

¹Institute of Geography and Oeschger Centre for Climate Change Research, University of Bern, Bern, Switzerland

²Federal Office for the Environment FOEN, Ittigen, Switzerland

³Professorship Ecoclimatology, Technical University of Munich, Freising, Germany

Correspondence: Céline Portenier (celine.portenier@giub.unibe.ch)

Abstract. Snow cover variability has a significant impact on climate and environment and is of great socio-economic importance for the European Alps. Terrestrial photography offers a high potential to monitor snow cover variability, but its application is often limited to the small catchment scale. Here, we present a semi-automatic procedure to derive snow cover maps from arbitrary webcam images. We use freely available webcam images of the Swiss Alps and propose a procedure for the georectification and snow classification of such images. In order to avoid the effort of manually setting ground control points (GCPs) for each webcam, we implement a new registration approach that automatically resolves camera parameters (camera orientation, principal point, field of view (FOV)) by using an estimate of the webcams position and a high-resolution digital elevation model (DEM). Furthermore, two recent snow classification methods are compared and analyzed. The resulting snow cover maps have the same spatial resolution as the DEM and indicate whether a grid cell is snow-covered, snow-free, or not visible from webcams' positions. GCPs were used to evaluate our novel automatic image registration approach. The evaluation reveals in a root mean square error (RMSE) of 14.1 m for standard lens webcams (FOV < 48°) and a RMSE of 36.3 m for wide-angle lens webcams (FOV ≥ 48°). Overall, our results highlight the potential of our method to built up a webcam-based snow cover monitoring network.

1 Introduction

Snow is an essential natural resource. Because snow has a much higher albedo compared to other natural land surfaces, its areal extent plays an important role in the Earth's energy balance. In alpine regions, snow plays a key role in the hydrologic cycle. It acts as water storage and accounts for a substantial proportion of the total runoff. Information about spatial and temporal snow distribution is therefore essential for monitoring water resources and predicting runoff (Jonas et al., 2009), and it is of crucial importance for water supply and hydropower production. In addition, seasonal snow cover not only plays an important role for the development of ecosystems but has a high economic value for winter tourism as well.

Most commonly used methods to monitor snow cover variability are based on in situ measurements and satellite remote sensing. In situ measurements, e.g., from ground-based monitoring networks, provide accurate and long time series of local snow sites and can be used, for example, for long-term trend analyses (e.g., Laternser and Schneebeli, 2003; Marty, 2008; Klein et al., 2016). These measurements, however, might not capture the spatial variability of snow cover. In contrast to in situ



measurements, remote sensing data can provide spatially comprehensive information on snow cover extent. In particular optical remote sensing is widely used to study snow cover variability (e.g., Foppa and Seiz, 2012; Hüsler et al., 2012; Metsämäki et al., 2012; Wunderle et al., 2016). The main limiting factor of optical remote sensing techniques is cloud coverage. According to Dumont and Gascoin (2016), the yearly average of pixels hidden by clouds is about 50% for the Pyrenees and 60% in the Austrian Alps. Large uncertainties exist in shadowed or forested areas. Moreover, the sensor resolution (e.g., 250 m or 1.1 km resolution of the MODIS and AVHRR sensor respectively) may limit the capture of small-scale variability of snow cover, especially in complex, mountainous terrain. The emergence of new techniques based on airborne digital photogrammetry and terrestrial photography enables to extract snow cover information with high spatial and temporal resolutions. Unmanned areal systems (UAS) enable the generation of high-resolution digital surface models that can be used to map the small scale variability of snow depth (e.g., Bühler et al., 2016; De Michele et al., 2016). However, UAS are often associated with high costs and its spatial coverage and temporal resolution is limited. In addition, weather constraints due to strong winds or precipitation can restrict the use of UAS, especially at high elevations.

In this work, we suggest the use of publicly available webcam images and present a semi-automatic procedure to generate snow cover maps from such images. This work builds on and extends the Master's thesis by Dizerens (2015). We focus on the Swiss Alps, where several thousands of public outdoor webcams are readily available online, resulting in a relatively dense sampling to study snow cover variability over a large area. Webcams are a cost-effective and efficient way to monitor snow cover variability in mountainous regions at very high spatio-temporal scales, and may offer detailed analyses of snow cover on steep slopes due to their oblique view on the mountains. Moreover, webcams can provide snow cover information even under cloudy weather conditions, and therefore, offer an unique potential for complementing satellite-derived snow information. The areal coverage, however, depends on the number of cameras used, their field of view (FOV), and their positioning in the field.

Terrestrial photography is an increasingly used observation method in different research disciplines such as glaciology (e.g., Corripio, 2004; Dumont et al., 2011; Huss et al., 2013; Messerli and Grinsted, 2015) and snow cover studies (e.g., Schmidt et al., 2009; Farinotti et al., 2010; Härer et al., 2013; Pimentel et al., 2014; Härer et al., 2016; Liu et al., 2015; Fedorov et al., 2016; Revuelto et al., 2016; Arslan et al., 2017; Millet et al., 2018). However, most of these studies use single cameras and thus are limited in areal coverage. In particular, they either require known camera parameters (i.e., extrinsic and intrinsic camera parameters such as the camera orientation or the FOV of the camera) or require significant manual user input (e.g., ground control points (GCPs)) to georectify terrestrial photography. Since camera parameters are not readily available for public webcams, and manually setting GCPs for a large number of cameras is time-consuming, these methods are of limited application for our purposes. Therefore, we implement a processing scheme that minimizes manual user input by automation.

Our georectification approach registers a webcam image with a digital elevation model (DEM). This image-to-DEM registration automatically resolves the required webcam parameters, such as the camera's orientation and its FOV by using an estimate of the webcams position only. Combined with existing snow classification approaches and our automatic image-to-image alignment, this procedure can be applied to arbitrary images to generate snow cover maps with a minimal effort. To assess the accuracy of our automatic snow cover mapping, we analyze and evaluate the components of the processing chain with a focus on automatic image-to-DEM registration, where manually selected GCPs are used to analyze the mapping error.

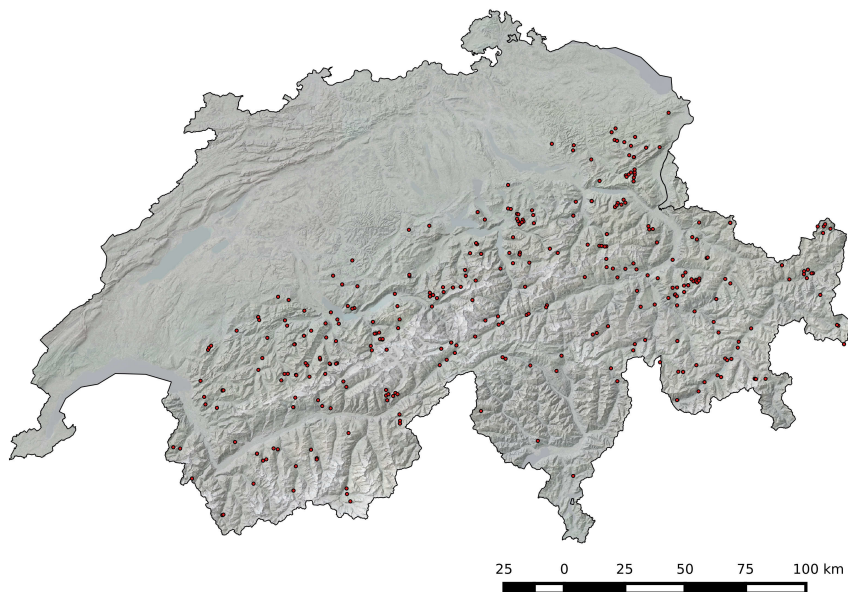


Figure 1. Locations of 297 webcams (red points) in the Swiss Alps. Background data: SWISSIMAGE and swissALTI3D by swisstopo.

This work is organized as follows: in Section 2, the webcam data, DEM, and orthophoto used in this work are described. In Section 3, we present the proposed methods of our procedure. Qualitative examples of snow cover maps and a comparison of the applied snow classification methods are shown in Section 4, followed by a detailed evaluation of the mapping accuracy in Section 5. Finally, we discuss the advantages and limitations of our procedure (Section 6), before concluding in Section 7.

5 2 Data

2.1 Webcam images

The website www.kaikowetter.ch offers a network of about 520 outdoor webcams observing the current snow conditions in and around Switzerland. Most of these webcams were installed by mountain railway operators, restaurants, hotels, and private citizens. They offer images within a one-hourly to 10-minute interval. Since November 2011, we are archiving one image per day of each webcam from this website and extend our archive continuously with webcam images from other web-sources. For this study, we select 297 webcams located in the Swiss Alps at elevations ranging from 800 m to 3900 m a.s.l. (see Fig. 1). All these webcams fulfill one main condition: the mountain silhouette is visible on the webcam image, i.e., it is not obscured by trees or buildings.

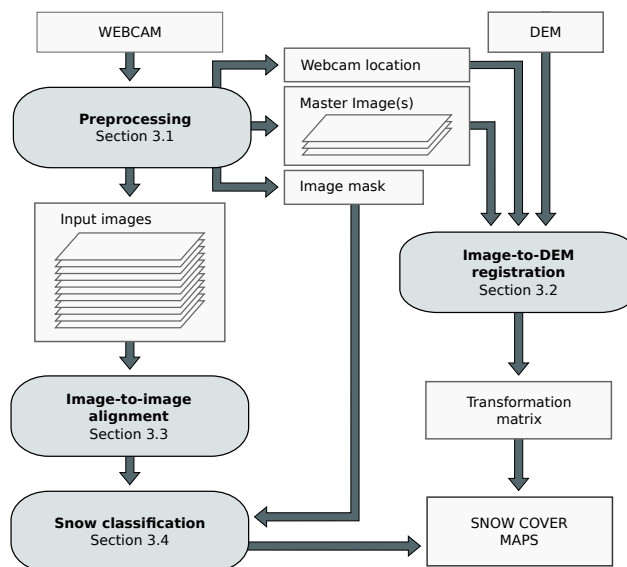


Figure 2. Overview of the proposed procedure. It consists of four major steps: preprocessing, automatic image-to-DEM registration, automatic image-to-image alignment, and automatic snow classification. Image-to-DEM registration results in a transformation matrix that is used to project the snow-classified pixels onto a map.

2.2 Swiss geodata

We use the swissALTI^{3D} DEM and the orthophoto SWISSIMAGE, produced by the Swiss Federal Office of Topography (swisstopo, 2013a, b). The DEM covers Switzerland and Liechtenstein and has a spatial resolution of 2 m. It was created using airborne laser scanning data (below 2000 m a.s.l.) or stereocorrelation of areal photographs (above 2000 m a.s.l.) and features an accuracy of 0.5 m and 1 to 3 m on average, respectively. The orthophoto SWISSIMAGE is composed of digital aerial orthophotographs of Switzerland, featuring a spatial resolution of 0.25 m in the Swiss Lowlands and 0.5 m in the Swiss Alps.

3 Methods

The proposed procedure consists of four major steps: preprocessing, automatic image-to-DEM registration, automatic image-to-image alignment, and automatic snow classification (see Fig. 2 for an overview). In the preprocessing step (Sect. 3.1), manual user input is required to estimate the webcam's location, to select a representative image for image-to-DEM registration (hereafter referred as Master Image), and to provide an image mask. Second, the selected Master Image is automatically registered with the DEM to derive the unknown camera parameters, such as orientation and FOV of the webcam (Sect. 3.2). Successful image-to-DEM registration results in a transformation matrix that relates each pixel of the Master Image to its 3D coordinates. Since an image series of a webcam is usually not perfectly aligned, we automatically align images to the selected



Master Image (Sect. 3.3). This enables the use of the same transformation matrix for all webcam images. Finally, each image is automatically snow-classified (Sect. 3.4). Using the transformation matrix, a georeferenced snow cover map can be generated.

3.1 Preprocessing

First, a webcam's location and its installation height above ground has to be estimated manually. This is achieved by considering the position of objects visible in the webcam image, the orthophoto SWISSIMAGE, and additional information provided by the webcam owner. In some cases, touristic photographs and images from Google Street View help to improve the location estimation. Up to now, we have estimated the locations of 297 webcams (see Fig. 1) with an estimated accuracy of about 5m. Next, at least one Master Image per webcam is selected. This image has to be representative for all other images of the same webcam, and should feature high contrast between the mountains and the sky for automatic image-to-DEM registration. Finally, a mask can be prepared to define image regions that should be ignored in the snow map generation procedure. Such regions can be trees, buildings, or other fixed infrastructure, and are defined on the Master Image.

3.2 Automatic image-to-DEM registration

The registration of an image with a DEM requires a common feature space. As in the study of Baboud et al. (2011) and Fedorov et al. (2016), we make use of mountain silhouettes, which are among the most salient structural features in mountainous natural environments. Gaussian filtering and Sobel edge detection are applied to the Master Image to reduce noise and extract the structural features from the images. Next, the mountain silhouette is automatically detected from the edge image (see Fig. 3). Our silhouette extraction is based on the assumption that the mountain silhouette is the uppermost edge line that spans the full width of the image. It starts at the top left pixel in the edge image and looks for the first edge pixel in the first column. Once a pixel is found, the algorithm iteratively searches in a 7×7 pixel neighborhood for other edge pixels until a continuous line is found that spans the full width of the image. If no such edge line is found, the algorithm starts again at the next edge pixel in the first column of the image.

To derive the unknown camera parameters, the extracted mountain silhouette is registered with mountain silhouettes extracted from virtually rendered DEM images. These DEM images are generated by projecting the DEM point cloud from its world coordinate system via a camera coordinate system to an image coordinate system (see Fig. 4 and 5) by using a pinhole camera model. To reduce the computational complexity, only DEM points that are visible from the point of view of the webcam are considered. For this purpose, the viewshed generation module of the Photo Rectification And Classification Software (PRACTISE V.1.0; Härer et al., 2013) is used to generate a 360° visibility map from the point of view of the webcam. The projected DEM points \mathbf{p}' of the virtual DEM image are computed by multiplying the visible DEM points \mathbf{p} by the inverse of a camera matrix \mathbf{C} , a perspective projection matrix \mathbf{P} , and a viewport matrix \mathbf{D} :

$$\mathbf{p}' = \mathbf{DPC}^{-1}\mathbf{p}. \quad (1)$$

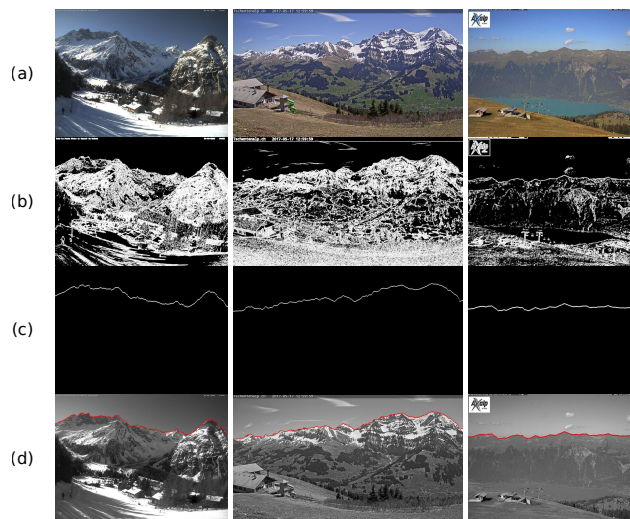


Figure 3. Examples of automatic silhouette extraction. (a) Webcam images, (b) extracted edges using Sobel edge detection, (c) detected mountain silhouettes, and (d) mountain silhouettes (red) superimposed on grayscale webcam images.

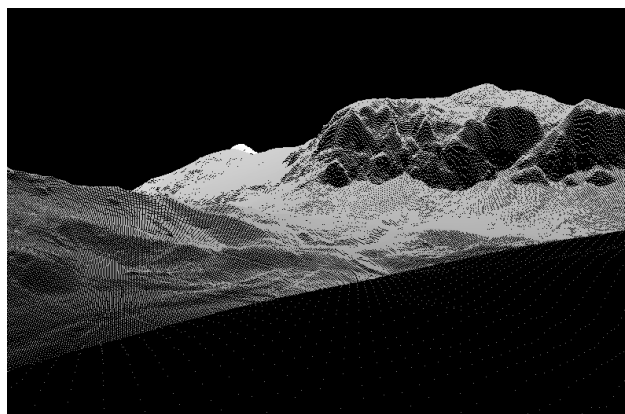


Figure 4. Sample rendering of a digital elevation model (DEM) using a pinhole camera model.

The camera matrix \mathbf{C} transforms from camera coordinates to world coordinates and is defined by extrinsic camera parameters, i.e., the camera's location and orientation with respect to the known world reference frame. It is given by

$$\mathbf{C} = \begin{bmatrix} \mathbf{x}_c & \mathbf{y}_c & \mathbf{z}_c & \mathbf{cop} \\ 0 & 0 & 0 & 1 \end{bmatrix}, \quad (2)$$

where \mathbf{cop} is the camera's location and \mathbf{x}_c , \mathbf{y}_c , and \mathbf{z}_c are the three vectors of the camera coordinate system that define its orientation, i.e., the roll, pitch, and yaw angle. The perspective projection matrix \mathbf{P} transforms objects into canonic view

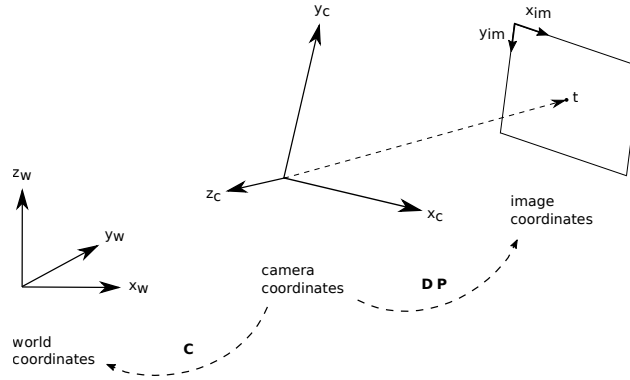


Figure 5. World, camera, and image coordinate systems and its transformations using camera matrix C , perspective projection matrix P , and viewport matrix D .

volume (i.e. a cube) so that the image points are normalized view coordinates in the range $[-1, 1] \times [-1, 1] \times [-1, 1]$. It is defined by intrinsic camera parameters and is given by

$$\mathbf{P} = \begin{bmatrix} \frac{1}{a \cdot \tan(FOV/2)} & 0 & 0 & 0 \\ 0 & \frac{1}{\tan(FOV/2)} & 0 & 0 \\ 0 & 0 & \frac{near+far}{near-far} & \frac{2 \cdot near \cdot far}{near-far} \\ 0 & 0 & -1 & 0 \end{bmatrix}, \quad (3)$$

where a is the image aspect ratio and $near$ and far are the distances to a near and a far plane that limit the infinite viewing volume. To finally transform to pixel coordinates $(x_{im}, y_{im}) \in [x_0 \dots x_1] \times [y_0 \dots y_1]$, the viewport matrix, given by

$$\mathbf{D} = \begin{bmatrix} (x_1 - x_0)/2 & 0 & 0 & (x_0 - x_1)/2 \\ 0 & (y_1 - y_0)/2 & 0 & (y_0 - y_1)/2 \\ 0 & 0 & 1/2 & 1/2 \\ 0 & 0 & 0 & 1 \end{bmatrix} \quad (4)$$

has to be applied. It scales the projected pixels to a certain image size and translates them so that the origin of the image coordinate system is at the upper left corner. Since we use homogeneous coordinates, we apply perspective division to obtain pixel coordinates. Using this camera model, virtual DEM images can be generated by sampling the unknown parameters (i.e., the three orientation vectors x_c , y_c , and z_c of the camera and the FOV).

To estimate the ground truth camera parameters, we propose a silhouette matching procedure. Similar to before, the mountain silhouettes are extracted from the rendered DEM images using the method described above. Given two silhouettes, i.e., the

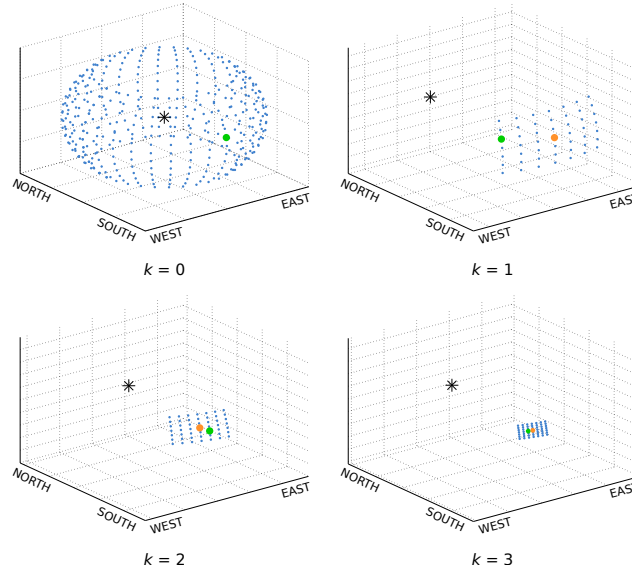


Figure 6. Viewing directions (blue points) of a camera (asterisk) during image-to-DEM registration. The green dots indicate the viewing directions with the best score, and the orange dots indicate the best viewing directions of the previous scale. An example is shown for vertical and horizontal rotations from scale $k = 0$ to $k = 3$.

Master Image silhouette and a silhouette extracted from a sampled DEM rendering, we define a score function based on 2D cross-correlation to quantify how well the two silhouettes match:

$$score = \alpha \cdot w_1 + (1 - \alpha) \cdot w_2, \quad (5)$$

where w_1 is the normalized maximum response of cross-correlation, and w_2 is the normalized image space offset defined by the distance between the pixel location of the maximum response and the image center. The final score is the weighted sum using a user-defined parameter α . To estimate the camera parameters, we seek for the parameters that maximize this score.

To efficiently search for the best matching silhouette pair, silhouette matching is performed on multiple scales k . On each scale, the algorithm rotates the camera coordinate system horizontally and vertically (see Fig. 6) and searches for the highest score. On scale i , the estimated parameters of scale $i - 1$ are used as initialization and is rotated n_x -times around the z -coordinate of the world coordinate system and n_y -times around the x -axis of the camera coordinate system. On scale $k = 0$, the parameters are initialized randomly. The horizontal and vertical rotation steps are called strides s_x and s_y respectively. On scale $k = 0$, we set an initial stride of $s_x = 360^\circ / n_x$ (with $n_x = 20$) and $s_y = 90^\circ / n_y$ (with $n_y = 12$). For all scales $k > 0$, the horizontal and vertical strides are recursively defined by

$$s_{x_i} = \frac{3s_{x_{i-1}}}{n_x} \text{ and } s_{y_i} = \frac{3s_{y_{i-1}}}{n_y}. \quad (6)$$



To approximate the roll angle of the camera, we additionally rotate the x-coordinate of the camera matrix on each scale $m = 5$ times around the viewing direction once the image space offset w_2 is smaller than 10 pixels. An initial stride of $s_m = 3^\circ/m$ is set and decreased each scale by

$$s_{m_k} = \frac{3s_{m_{k-1}}}{m}. \quad (7)$$

5 Instead of estimating the FOV manually, our procedure can also optimize the FOV of the webcam by first iterating the horizontal FOV of 30° by 5° to a FOV of 90° in scale $k = 0$. The best matching silhouette pair defines the initial FOV estimate. Once the image space offset w_2 is smaller than 20 pixels, the FOV can be estimated more accurately by evaluating different FOVs at each iteration: the FOV is iterated at each viewing direction $f = 5$ times around the initial FOV with an initial stride $s_{FOV} = 2^\circ$, decreasing each scale by

$$10 \quad s_{f_k} = \frac{3s_{f_{k-1}}}{f}. \quad (8)$$

The weighting parameter α (Eq. 5) is a function of scale k . On scale $k = 0$, we set $\alpha = 1$, such that the final score is mainly determined by the maximum response of cross-correlation w_1 . The normalized image space offset w_2 is ignored, since it would mainly correspond to an offset of a wrongly matched silhouette pair. w_2 becomes important for scales $k > 0$, once the viewing direction estimate is reasonably accurate. The smaller the distance of the maximum response to the image center, the better the
15 two silhouettes match. Therefore, α is set to a low value (0.1). Once the roll angle and FOV is resolved, both measures, w_1 and w_2 , are set equally ($\alpha = 0.5$), since both the smallest offset and the highest response value have to be estimated.

To find the best score efficiently, the virtual DEM images are rendered with a lower resolution in the first scales. Starting with a width of $w = w_{orig}/8$ and height of $h = h_{orig}/8$ in scale $k = 0$, the width and height are doubled until the original image size is reached in scale $k = 3$. Experiments have shown that image-to-DEM registration requires around 12 scales until the best
20 matching silhouette pair with an image space offset of 0 is found. This best matching silhouette pair results in a transformation matrix that relates each pixel of the Master Image to its real 3D coordinates.

3.3 Automatic image-to-image alignment

Because image-to-DEM registration is computationally expensive and mountain silhouettes cannot be detected on each webcam image due to cloud cover or low contrast conditions, each webcam image is automatically aligned to its Master Image by
25 solving for a homography \mathbf{H} . A homography is a projective transformation between two images with the same camera position but different orientation and is used to relate the two images so that they can be aligned.

We use the Scale Invariant Feature Transform (SIFT; Lowe, 2004) to detect structural features in a webcam image and its corresponding Master Image. It transforms an image into a collection of local feature vectors that consist of a SIFT keypoint (image location) and a SIFT descriptor that is highly distinctive and invariant to illumination, position, and scale. After the
30 feature detection, the features are matched across the two images (see Fig. 7). The similarity between two feature vectors is given by their Euclidean distance. Since the number of potential matching features can be quite large, we approximate this distance using an algorithm called Best-Bin-First (see Lowe, 2004). We use the SIFT implementation from the open source library VLFeat (Vedaldi and Fulkerson, 2010).

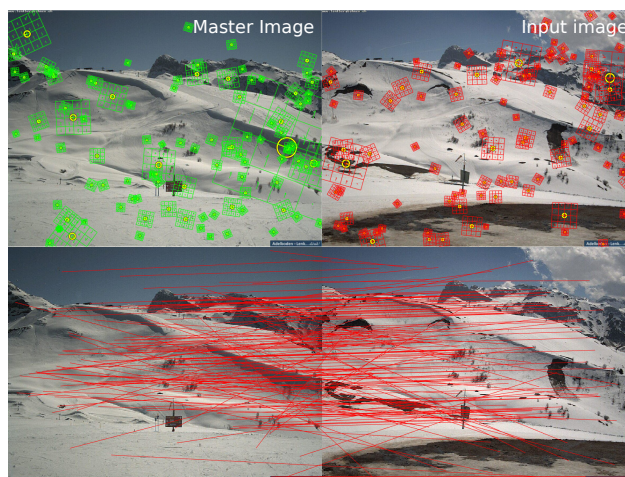


Figure 7. SIFT features of a Master Image and an input image and corresponding matches between all features. To simplify the illustration, we show a subset of 100 randomly selected SIFT features per image.



Figure 8. Example of an arbitrary input image that is aligned to a corresponding Master Image. The mountain silhouette extracted from the Master Image is shown in red.



A homography \mathbf{H} is a 3×3 matrix. Since scale is arbitrary, \mathbf{H} has eight unknown parameters. Therefore, at least four point correspondences (x/y image coordinates) are needed to solve for \mathbf{H} . Since not all matched pairs are correct, the homography is estimated using the best matching feature points. For this purpose, we use the robust fitting model RANdom SAMple Consensus (RANSAC; Fischler and Bolles, 1981). RANSAC randomly selects four pairs of corresponding points to calculate the homography, transforms all points from one image to the other using the found homography, and searches for the solution that has the best agreement with all remaining matching pairs. This best agreement is found by calculating the mapping error between each transformed SIFT point of an input image and its corresponding SIFT point of the Master Image. To eliminate the bias towards any particular set of points, the best matching image-to-image alignment is achieved by recalculating the homography using all features with a small mapping error of the best homography found by RANSAC. Figure 8 shows an example of an image that is aligned to a corresponding Master Image.

3.4 Automatic snow classification

We perform experiments using two recent snow classification methods. The first method by Salvatori et al. (2011) analyses the blue band frequency histogram to set a snow threshold. This threshold is automatically selected at the histogram's first local minimum above the intensity value 127. If no local minimum is found, the snow threshold is set to the value 127. All pixel values equal or higher than this threshold value are classified as snow, whereas lower values are classified as snow-free.

The second method is a snow classification routine included in PRACTISE V.2.1 (Härer et al., 2016). Since the method by Salvatori et al. (2011) works only reasonably well for non-shadowing areas (Härer et al., 2016; Arslan et al., 2017), this routine additionally detects snow in the shaded regions of an image. After applying the blue-band classification proposed by Salvatori et al. (2011), Härer et al. (2016) refine snow classification using principal component analysis (PCA) for separating shaded snow cover from sunlit rock surfaces. We refer to Härer et al. (2016) for more details.

The snow classification takes as input a webcam image and the corresponding image mask described in Section 3.1. Additionally, all sky pixels are automatically masked out using the mountain silhouette extracted from the Master Image. An example of snow classification is shown in Fig. 9.

4 Snow cover maps

The transformation matrix found for each Master Image is used to project the snow-classified pixels onto a georeferenced map. The resulting snow cover map has the same resolution as the DEM. Figure 10 shows two webcam images in the region of the Metschalp on 6 March and 5 May 2015 and resulting snow cover maps. These maps indicate for each grid cell whether it is snow-covered, snow-free, or not visible from webcam's position.

Our procedure facilitates snow cover analyses using arbitrary terrestrial images. Figure 11 reveals the percentage of snow covered area on a mountain hill in the Furkapass region from 14 April to 28 August 2015 and three example images with applied classifications. Webcam images containing fog or adverse cloud cover that impede the view were removed before processing. The differences caused by the two classification methods are discussed in Sect. 6.

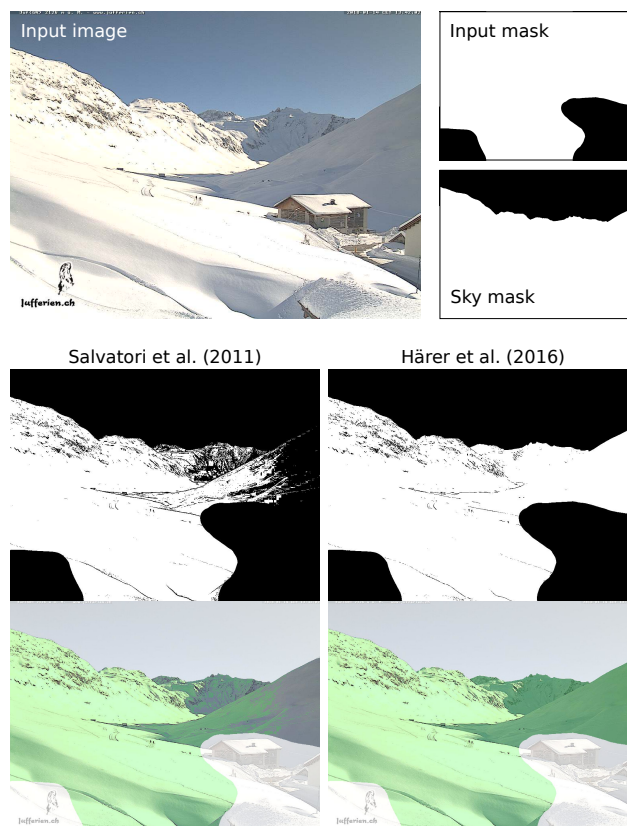


Figure 9. Example of a webcam image that is masked for subsequent snow classification using an input mask and a sky mask derived from the extracted mountain silhouette. Snow classification is applied using the methods by Salvatori et al. (2011) and Härer et al. (2016). Detected snow is shown in white in the binary output image (black: no snow or masked out) and a transparent green layer on the original webcam image (white transparent layer: masked region).

5 Evaluation

In this section, we present an evaluation of our automatic image-to-DEM registration. We apply image-to-DEM registration on 50 Master Images. Our silhouette extraction technique successfully detects all 50 silhouettes. For 5 webcams, automatic image-to-DEM registration fails to find the appropriate orientation of the camera. This failure is either caused by heavy lens distortions of the camera system or due to several excerpts of similar looking mountain silhouettes that lead to a wrong orientation estimate on scale $k = 0$.

To evaluate the accuracy of our automatic image-to-DEM registration, we select 20 webcams that comprise different areal extents and lens characteristics. Depending on the presence of structural image content, we manually select 5 to 15 GCPs per webcam using the SWISSIMAGE orthophoto. For 142 GCPs in total, we calculate the root mean square error (RMSE) of the distance between the real and projected GCPs and its relative pixel error in image space (percentage of image width/height)

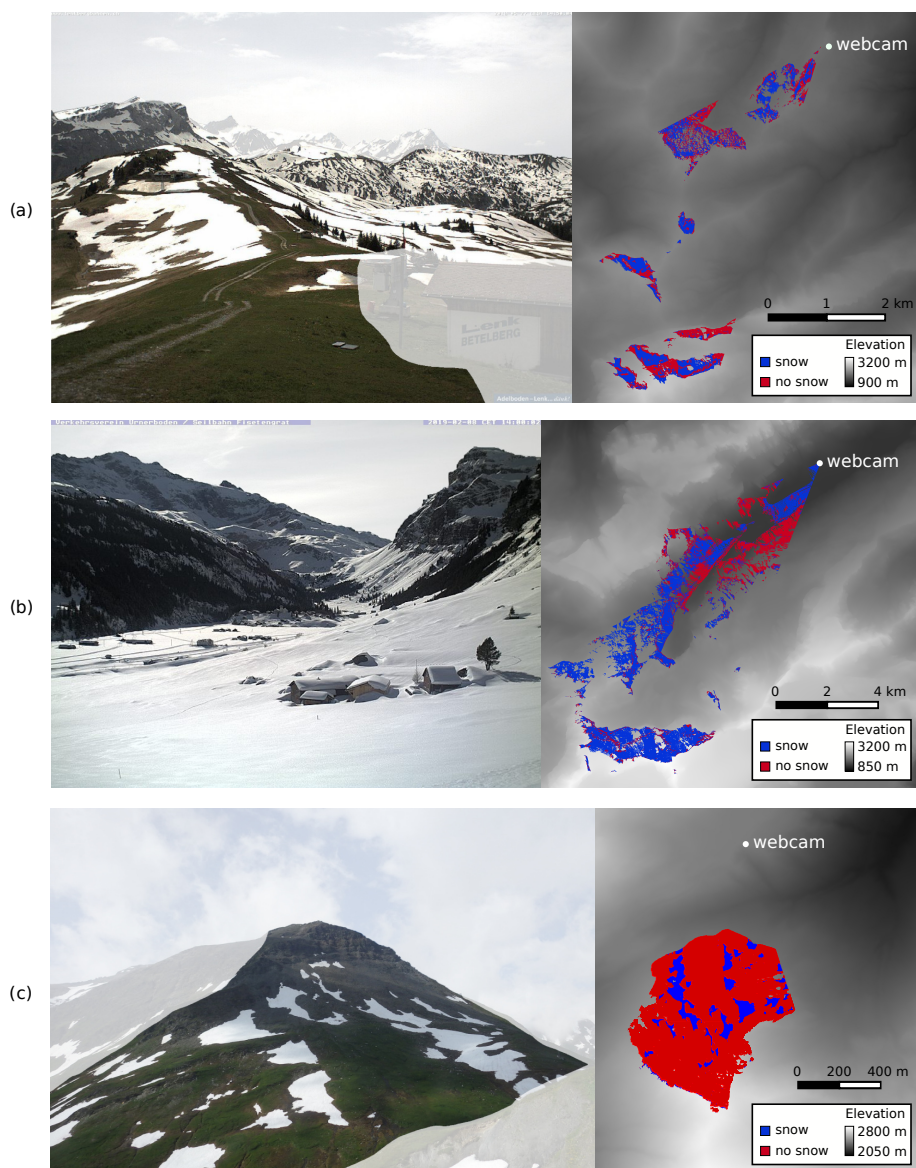


Figure 10. Example webcam images and resulting snow cover maps of three webcams in the (a) Lenk, (b) Urnerboden, and (c) Furkapass region. The grayscale values of the snow cover maps shows the elevation values of the area that is not visible from the webcam's location.

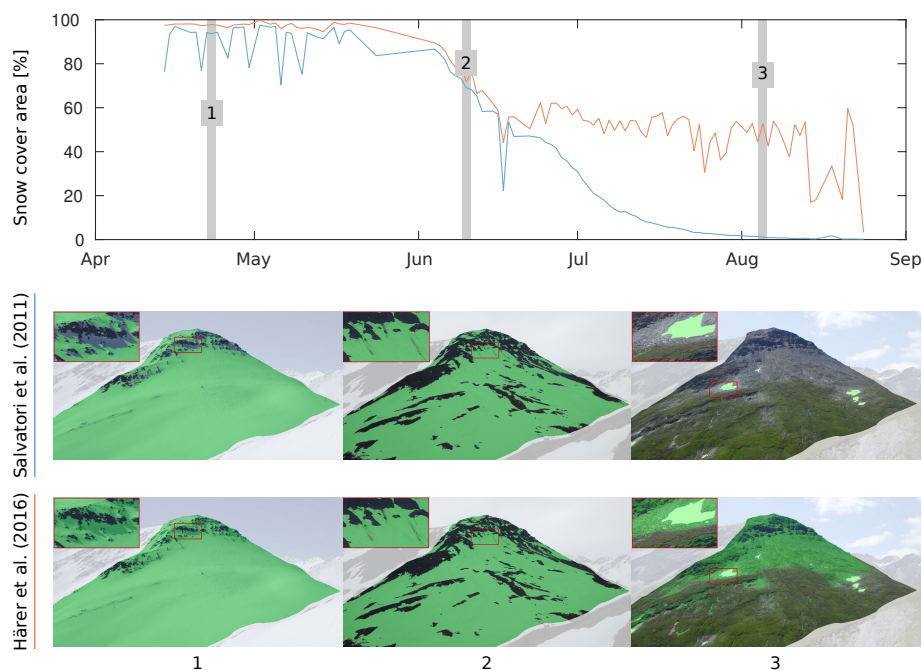


Figure 11. Percentage of snow covered area on a mountain hill in the Furkapass region from 14 April to 28 August 2015 using the snow classification proposed by Salvatori et al. (2011) and Härer et al. (2016).

(see Table 1). We find a significant difference in the mapping accuracy between webcams equipped with standard lenses (FOV <math>< 48^\circ</math>) and wide-angle lenses (FOV $\geq 48^\circ$). Our evaluation reveals an overall RMSE of 23.7 m, with a RMSE of 14.1 m for standard lens webcams and 36.3 m for wide-angle lens webcams. This difference is mainly caused by lens distortions, which increase with a larger FOV and therewith lead to a discrepancy of the silhouette matching, mainly at the outer part of the images. This discrepancy is even more prominent when considering the relative pixel error by comparing GCPs at the mountain silhouette, GCPs that are close to the image border (the outer 25% of the total image width/height), and the remaining GCPs in the center region of the image (see Fig. 12). The relative pixel error is notably higher for GCPs at the border of the images than the remaining GCPs, especially for wide-angle lens webcams. Not surprisingly, smallest errors are found for GCPs located at the mountain silhouette, since this silhouette is used for image-to-DEM registration. This indicates the effectiveness of our proposed silhouette-based image-to-DEM registration.

In Fig. 13, box plots of the distance error between the real and projected GCPs are shown for standard and wide-angle lens webcams. Results are grouped into three categories of GCPs within 0–2 km, 2–6 km, and 6–30 km distance to the webcam. It can be clearly seen that the largest residuals are caused by GCPs of wide-angle lens webcams that are located close to the webcam (0–2 km) and that the residuals generally decrease with the distance to the webcam. For standard lens webcams, there is no considerable difference in the distance error between GCPs within 0–2 km and 2–6 km distance to the webcam. For both, standard lens and wide-angle lens webcams, the distance error of GCPs that are more than 6 km away from the webcam is



Table 1. Projection error of ground control points (GCPs) in standard lens (FOV < 48°) and wide-angle lens (FOV ≥ 48°) webcam images.

	#cams	#GCPs	GCP RMSE [m]	Minimum residual [m]	Maximum residual [m]	σ RMSE [[m]	Relative pixel error [%]
All GCPs	20	142	23.70	2.00	98.48	17.06	0.74
GCPs standard lenses	14	96	14.10	2.00	34.97	8.67	0.61
GCPs wide-angle lenses	6	46	36.31	2.03	98.48	23.63	1.00

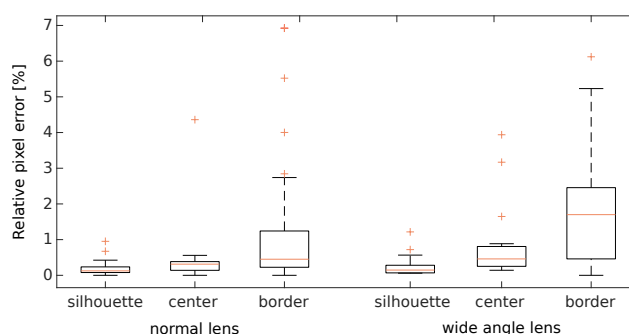


Figure 12. Relative pixel error of ground control points (GCPs) of standard and wide-angle lens webcams. Results are grouped in GCPs located at the mountain silhouette, the center region of the image, and the border region of the image (the outer 25 % of the total image width and height).

rather low (mean error distance of 8.6 m and 10.2 m, respectively) as most of these GCPs are located at the mountain silhouette, which is used for image-to-DEM registration.

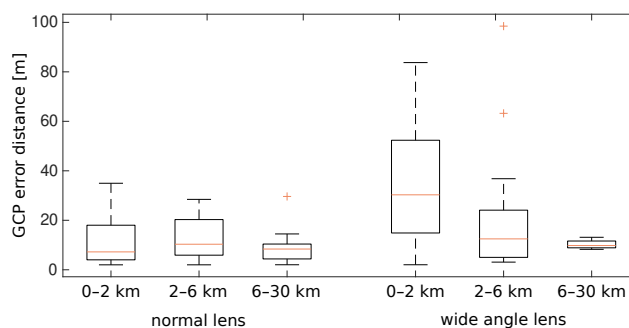


Figure 13. Distance error of the real and projected ground control points (GCPs) for standard and wide-angle lens webcams. Results are grouped in GCPs within 0–2 km, 2–6 km, and 6–30 km distance to the webcam.



6 Discussion

The performance of our automatic image-to-DEM registration procedure is promising. With marginal manual user input, we can transform an arbitrary webcam image into a georeferenced map. With an overall RMSE of about 23.7 m, our method is precise enough to validate or complement satellite-derived snow cover maps and offers snow cover analyses with a high spatio-temporal resolution over a large area. The large differences of RMSE between standard lens webcams and wide-angle lens webcams suggest a further improvement of our camera model to account for lens distortions. Given the large amount of webcams, we can also exclude webcams equipped with wide-angle lenses from analyses to notably reduce mapping errors (RMSE of 14.1 m found for 14 webcams equipped with standard lenses, see Table 1). Another solution is to use only the central part of an image if the FOV of the webcam is higher than a certain threshold.

Our method relies on a precise estimation of the webcam location. Especially when a decreasing slope is visible in the near field of the webcam, significant mapping errors may occur. For example, a too low estimate of the installation height may cause a pixel in 10 m distance to be mapped onto the counter slope 2 km away. Therefore, we recommend to mask out regions that are on the same slope as the webcam itself or areas close to edges with huge depth differences.

In general, we propose to mask out regions that are close to the webcam to avoid large mapping errors as shown in Figure 13 for webcams with wide-angle lenses. These large mapping errors may be caused by an imprecise location estimation. However, this effect was not observed for standard lens webcams. Hence, the large mapping errors close to the webcam can be attributed to the fact that close GCPs are generally more often located at the outer part of the image where lens distortions increase. In addition, areas closer to a webcam may generally have larger uncertainties as only the mountain silhouette is used for the image-to-DEM registration. Therefore, we can conclude that the mapping error is smaller the closer a pixel is to the mountain silhouette.

For most webcams, an intentional, significant change in its orientation occurs only occasionally and therefore, a landscape can be analyzed over a long time period in the case of an available image archive. Our image-to-image alignment enables to precisely correct small changes in orientation of webcam images and works generally well for images with similar image content. Alignment artifacts from e.g. logos in the image are eliminated by using RANSAC. Since some errors may occur if the image content differs too much, we propose not to align snowy winter images to snow-free images scenes and vice versa.

The snow classification method proposed by Salvatori et al. (2011) is frequently used and discussed in recent studies. Many of these studies emphasize the problem of misclassifications due to snow in shadowing regions (e.g. Härer et al., 2016; Arslan et al., 2017; Salzano et al., 2019). We have observed the same issue, especially for winter scenes with a low solar zenith angle. The comparison with the snow classification method proposed by Härer et al. (2016) reveals a similar pattern for all the processed webcams. The method by Salvatori et al. (2011) is underestimating snow cover, mainly in shadowing areas (see Fig. 11 for an example). For snowy winter scenes, the PCA method by Härer et al. (2016) performs excellent and is able to correctly classify snow cover in shadowing areas. However, once less than about 50% of snow is present in an image, the method overestimates snow cover and classifies rock, trees or grass as snow (see Fig. 11). This is often observed when no shaded snow cover is present or in the case of strong illumination conditions. As shadows from structural terrain become less



in spring, the method of Salvatori et al. (2011) often only weakly underestimates the snow cover. For rare cases of very low illumination conditions, both methods fail to correctly classify snow.

Currently, we use a combination of both methods to get the best possible snow classification result. However, there is a need for an improved snow classification method. This method should be able to classify snow under varying illumination conditions and ideally can distinguish between snow and clouds or fog.

The differentiation between snow, clouds, and fog currently remains an unsolved problem for RGB images. Even though webcams are often located below the cloud cover, low clouds and fog in front of the landscape have to be removed manually to not falsify snow classification. Whereas fog can be automatically detected for cases where it is covering a substantial part of the image, clouds and fog that impede the view on a smaller part of the landscape are difficult to distinguish from snow.

Since our approach requires a visible mountain silhouette, it is not suited for webcams that observe flat areas. Moreover, there are geographical limitations since webcams might not be installed in very remote areas. Generally, a large-scale coverage of a region might be only possible in developed countries. Nevertheless, the high number of freely available webcams offers a unique potential for complementing satellite-derived snow cover information. For example, our webcam snow cover maps facilitate the gapfilling of partly cloud-obscured satellite-based snow cover maps or improve snow classification in steep terrain or shadow-affected image scenes.

7 Conclusions

We present a semi-automatic procedure to derive snow cover maps from freely available webcam images in the Swiss Alps. Our registration approach automatically estimates webcams' parameters, which allows to relate pixels of a webcam image to their real-world coordinates. Additionally, we use a method for automatic image-to-image alignment and compare two recent snow classification methods. A detailed evaluation of the automatic georectification is carried out and reveals in a RMSE of 23.7 m, with a RMSE of 14.1 m for webcams equipped with standard lenses and 36.3 m for webcams equipped with wide-angle lenses. To the best of our knowledge, no other method is able to offer this accuracy on such a high spatio-temporal resolution over a large area. Large accuracy differences between standard lens webcams and webcams equipped with wide-angle lenses suggest to improve our camera model to incorporate effects of lens distortions or to use only the central part of an image to generate more accurate snow cover maps. However, an improvement of RGB snow classification is essential to automatically derive snow cover maps, i.e. to avoid the manual removal of cloudy scenes. Nevertheless, our approach offers snow cover analyses with a high spatio-temporal resolution over a large area with a minimum of manual user input. Our webcam-based snow cover monitoring network could not only serve as a reference for improved validation of satellite-based approaches, but also complement satellite-based snow cover retrieval.



Author contributions. Céline Portenier developed the code and performed the data analysis with advice from Fabia Hüsler and Stefan Wunderle. Stefan Härer provided matlab code of the software PRACTISE. Céline Portenier wrote the manuscript with contributions from all co-authors.

Competing interests. The authors declare that they have no conflict of interest.

- 5 *Acknowledgements.* The digital elevation model swissALTI^{3D} and the orthophoto SWISSIMAGE were obtained from the Federal Office of Topography (swisstopo). The authors acknowledge Kai Kobler for providing updated webcam images on www.kaikowetter.ch and all webcam owners that provide their images online, in particular Armin Rist and Sara Fischer. Further we gratefully acknowledge Simon Gascoin and Tiziano Portenier for their constructive comments on the manuscript.



References

- Arslan, A. N., Tanis, C. M., Metsämäki, S., Aurela, M., Böttcher, K., Linkosalmi, M., and Peltoniemi, M.: Automated Webcam Monitoring of Fractional Snow Cover in Northern Boreal Conditions, *Geosciences*, 7, <https://doi.org/10.3390/geosciences7030055>, 2017.
- Baboud, L., Čadík, M., Eisemann, E., and Seidel, H.: Automatic photo-to-terrain alignment for the annotation of mountain pictures, in: CVPR 2011, pp. 41–48, <https://doi.org/10.1109/CVPR.2011.5995727>, 2011.
- 5 Bühler, Y., Adams, M. S., Bösch, R., and Stoffel, A.: Mapping snow depth in alpine terrain with unmanned aerial systems (UASs): potential and limitations, *The Cryosphere*, 10, 1075–1088, <https://doi.org/10.5194/tc-10-1075-2016>, 2016.
- Corripio, J. G.: Snow surface albedo estimation using terrestrial photography, *Int. J. Remote Sens.*, 25, 5705–5729, <https://doi.org/10.1080/01431160410001709002>, 2004.
- 10 De Michele, C., Avanzi, F., Passoni, D., Barzaghi, R., Pinto, L., Dosso, P., Ghezzi, A., Gianatti, R., and Della Vedova, G.: Using a fixed-wing UAS to map snow depth distribution: an evaluation at peak accumulation, *The Cryosphere*, 10, 511–522, <https://doi.org/10.5194/tc-10-511-2016>, 2016.
- Dizerens, C.: Georectification and snow classification of webcam images: potential for complementing satellite-derived snow maps over Switzerland, Master's thesis, Faculty of Science, University of Bern, Switzerland, 2015.
- 15 Dumont, M. and Gascoin, S.: 4 - Optical Remote Sensing of Snow Cover, in: *Land Surface Remote Sensing in Continental Hydrology*, edited by Baghdadi, N. and Zribi, M., pp. 115–137, Elsevier, <https://doi.org/10.1016/B978-1-78548-104-8.50004-8>, 2016.
- Dumont, M., Sirguey, P., Arnaud, Y., and Six, D.: Monitoring spatial and temporal variations of surface albedo on Saint Sorlin Glacier (French Alps) using terrestrial photography, *The Cryosphere*, 5, 759–771, <https://doi.org/10.5194/tc-5-759-2011>, 2011.
- Farinotti, D., Magnusson, J., Huss, M., and Bauder, A.: Snow accumulation distribution inferred from time-lapse photography and simple modelling, *Hydrol. Process.*, 24, 2087–2097, <https://doi.org/10.1002/hyp.7629>, 2010.
- 20 Fedorov, R., Camerada, A., Fraternali, P., and Tagliasacchi, M.: Estimating Snow Cover From Publicly Available Images, *IEEE T Multimedia*, 18, 1187–1200, <https://doi.org/10.1109/TMM.2016.2535356>, 2016.
- Fischler, M. A. and Bolles, R. C.: Random Sample Consensus: A Paradigm for Model Fitting with Applications to Image Analysis and Automated Cartography, *Commun. ACM*, 24, 381–395, <https://doi.org/10.1145/358669.358692>, 1981.
- 25 Foppa, N. and Seiz, G.: Inter-annual variations of snow days over Switzerland from 2000–2010 derived from MODIS satellite data, *The Cryosphere*, 6, 331–342, <https://doi.org/10.5194/tc-6-331-2012>, 2012.
- Härer, S., Bernhardt, M., Corripio, J. G., and Schulz, K.: PRACTISE – Photo Rectification And ClassificaTIon SoftwarE (V.1.0), *Geosci. Model Dev.*, 6, 837–848, <https://doi.org/10.5194/gmd-6-837-2013>, 2013.
- Härer, S., Bernhardt, M., and Schulz, K.: PRACTISE – Photo Rectification And ClassificaTIon SoftwarE (V.2.1), *Geosci. Model Dev.*, 9, 307–321, <https://doi.org/10.5194/gmd-9-307-2016>, 2016.
- 30 Hüsler, F., Jonas, T., Wunderle, S., and Albrecht, S.: Validation of a modified snow cover retrieval algorithm from historical 1-km {AVHRR} data over the European Alps, *Remote Sens. Environ.*, 121, 497–515, <https://doi.org/10.1016/j.rse.2012.02.018>, 2012.
- Huss, M., Sold, L., Hoelzle, M., Stokvis, M., Salzmann, N., Farinotti, D., and Zemp, M.: Towards remote monitoring of sub-seasonal glacier mass balance, *Ann. Glaciol.*, 54, 75–83, <https://doi.org/doi:10.3189/2013AoG63A427>, 2013.
- 35 Jonas, T., Marty, C., and Magnusson, J.: Estimating the snow water equivalent from snow depth measurements in the Swiss Alps, *J. Hydrol.*, 378, 161–167, <https://doi.org/10.1016/j.jhydrol.2009.09.021>, 2009.



- Klein, G., Vitasse, Y., Rixen, C., Marty, C., and Rebetez, M.: Shorter snow cover duration since 1970 in the Swiss Alps due to earlier snowmelt more than to later snow onset, *Clim. Change*, 139, 637–649, <https://doi.org/10.1007/s10584-016-1806-y>, 2016.
- Laternser, M. and Schneebeli, M.: Long-term snow climate trends of the Swiss Alps (1931–99), *Int. J. Climatol.*, 23, 733–750, <https://doi.org/10.1002/joc.912>, 2003.
- 5 Liu, J.-f., Chen, R.-s., and Wang, G.: Snowline and snow cover monitoring at high spatial resolution in a mountainous river basin based on a time-lapse camera at a daily scale, *J. Mt. Sci.*, 12, 60–69, <https://doi.org/10.1007/s11629-013-2842-y>, 2015.
- Lowe, D. G.: Distinctive Image Features from Scale-Invariant Keypoints, *Int. J. Comput. Vis.*, 60, 91–110, <https://doi.org/10.1023/B:VISI.0000029664.99615.94>, 2004.
- Marty, C.: Regime shift of snow days in Switzerland, *Geophys. Res. Lett.*, 35, <https://doi.org/10.1029/2008GL033998>, 2008.
- 10 Messerli, A. and Grinsted, A.: Image georectification and feature tracking toolbox: ImGRAFT, *Geosci. Instrumentation, Methods Data Syst.*, 4, 23–34, <https://doi.org/10.5194/gi-4-23-2015>, 2015.
- Metsämäki, S., Mattila, O.-P., Pulliainen, J., Niemi, K., Luojuus, K., and Böttcher, K.: An optical reflectance model-based method for fractional snow cover mapping applicable to continental scale, *Remote Sens. Environ.*, 123, 508–521, <https://doi.org/10.1016/j.rse.2012.04.010>, 2012.
- 15 Millet, P., Huwald, H., and Weijs, S. V.: Extracting High Resolution Snow Distribution Information with Inexpensive Autonomous Cameras, in: HIC 2018. 13th Int. Conf. Hydroinformatics, edited by Loggia, G. L., Freni, G., Puleo, V., and Marchis, M. D., vol. 3 of *EPiC Series in Engineering*, pp. 1397–1405, EasyChair, <https://doi.org/10.29007/93gh>, 2018.
- Pimentel, R., Pérez-Palazón, M. J., Herrero, J., and Polo, M. J.: Monitoring Snow Cover Area In Semiarid Regions Using Terrestrial Photography, *Int. Conf. Hydroinformatics*, Paper 378, 2014.
- 20 Revuelto, J., Jonas, T., and López-Moreno, J.-I.: Backward snow depth reconstruction at high spatial resolution based on time-lapse photography, *Hydrol. Process.*, 30, 2976–2990, <https://doi.org/10.1002/hyp.10823>, 2016.
- Salvatori, R., Plini, P., Giusto, M., Valt, M., Salzano, R., Montagnoli, M., Cagnati, A., Crepaz, G., and Sigismondi, D.: Snow cover monitoring with images from digital camera systems, *Ital. J. Remote Sens.*, 43, 137–145, <https://doi.org/10.5721/ItJRS201143211>, 2011.
- Salzano, R., Salvatori, R., Valt, M., Giuliani, G., Chatenoux, B., and Ioppi, L.: Automated Classification of Terrestrial Images: The Contribution to the Remote Sensing of Snow Cover, *Geosciences*, 9, <https://doi.org/10.3390/geosciences9020097>, 2019.
- 25 Schmidt, S., Weber, B., and Winiger, M.: Analyses of seasonal snow disappearance in an alpine valley from micro- to meso-scale (Loetschental, Switzerland), *Hydrol. Process.*, 23, 1041–1051, <https://doi.org/10.1002/hyp.7205>, 2009.
- swisstopo: swissALTI3D, The high precision digital elevation model of Switzerland, https://shop.swisstopo.admin.ch/en/products/height_models/alti3d, last access: 27 March 2019, 2013a.
- 30 swisstopo: SWISSIMAGE, The Digital Color Orthophotomosaic of Switzerland, https://shop.swisstopo.admin.ch/en/products/images/ortho_images/SWISSIMAGE, last access: 27 March 2019, 2013b.
- Vedaldi, A. and Fulkerson, B.: Vlfeat: An Open and Portable Library of Computer Vision Algorithms, in: *Proc. 18th ACM Int. Conf. Multimed.*, pp. 1469–1472, ACM, New York, NY, USA, <https://doi.org/10.1145/1873951.1874249>, 2010.
- Wunderle, S., Gross, T., and Hüsler, F.: Snow Extent Variability in Lesotho Derived from MODIS Data (2000–2014), *Remote Sens.*, 8, <https://doi.org/10.3390/rs8060448>, 2016.